CONCRETE SURFACE TEMPERATURE MAPPING AND ANOMALY DETECTION WITH AIRBORNE THERMAL REMOTE SENSING

Ryo Michishita [a, b], Tadashi Sasagawa [a] and Peng Gong [b]

[a] PASCO Corporation, 1-1-2 Higashiyama, Meguro-ku, Tokyo, 153-0043, Japan
- (ryo_michishita, tadashi_sasagawa)@pasco.co.jp
[b] Center for the Assessment and Monitoring of Forest and Environmental Resources (CAMFER), UC Berkeley, 151 Hilgard Hall, Berkeley, CA, 94720-3110, U.S.A. - gong@nature.berkeley.edu

ABSTRACT:
Erosion control is one of the most important land development policies in Japan. Corrosion of concrete structures and associated structural failures can be seen in complex urban areas due to the difficulties in detection and maintenance of them. It is particularly true along transportation systems where retaining walls along highways are unstable. Early detection of such corroded spots possibly will prevent a significant amount of structural failures and loss. The objective of this study is to develop a temperature mapping algorithm that detects such anomalies in concrete structures through airborne thermal remote sensing. A new airborne thermal sensor, Thermal Airborne Broadband Imager (TABI), available at PASCO Corporation is utilized to acquire thermal data at 0.1 ^{o}C thermal resolution and with 1.5 m resolution for a study site in Japan. The shadow effect on radiant temperature was analyzed. The statistical T-test was used as measure in detecting concrete anomalies and proved to be effective.

KEY WORDS: Thermal, Mapping, Detection, Engineering, Aerial, Infrared

1. INTRODUCTION

The Japanese government puts a great deal of effort on erosion control. Concrete diagnosis is one of the most noteworthy topics. Thermography and non-contact thermometer are used for testing concrete conditions. However, it is consuming time and expensive to test vast areas and large structures. Measurement in undeveloped area using these kinds of equipments is almost impossible.

Thermal remote sensing data have been used for the land surface temperature monitoring in many application area including urban studies, climatology, and soil. Quattrochi (1999) studied the measurement and assessment of urban environment. Ben-Dor (1997) estimated the effect of urban heat island using thermal data. Ramsay (1999) developed a new method for volcanic mapping.

The objective of this study is to develop a temperature mapping algorithm that detects the anomalies in concrete structures through airborne thermal remote sensing. Such anomalies may cause temperature differences. In this paper, we investigate the applicability of airborne thermal remote sensing data for mapping concrete structure anomalies mapping in detecting temperature differences.

2. STUDY AREA AND THERMAL DATA ACQUISITION

Kono-Takefu is located in a mountainous area at the center of Fukui Pref. in Japan as shown in Fig. 1. Since the occurrence of a large-scale landslide in July 1989, many erosion facilities have been built in this region. We select a study area along the national road #8.

Thermal Airborne Broadband Imager 320 (TABI-320), a new airborne thermal sensor developed by ITRES Research Ltd. (Canada), was acquired by PASCO Corporation (Japan) in July 2003 and utilized to acquire the thermal data in October 2003 over this study site. The specifications of TABI are shown in Table. 1.

Table 2 lists the flight record of TABI for acquiring the thermal data with 1.5 m Ground Sampling Distance (GSD) in early afternoon (EA) and in early morning (EM). The study area covers 0.67 km * 7.2 km. These images were orthorectified with a 50 m resolution DEM released by Geographical Survey Institute of Japan. No atmospheric correction was done. Two strips of 1.5 m TABI images were mosaiced together. Fig. 2 shows the acquired TABI images based on parameters shown in Table. 2.

3. THERMAL BEHAVIOR OF LAND COVER MATERIALS

Fig. 3 shows the thermal behavior of land cover materials. In general, the temperature of each surface cover increases after sunrise, continues to increase until 2:00 PM, and then decreases gradually. The temperature deviation depends on surface cover

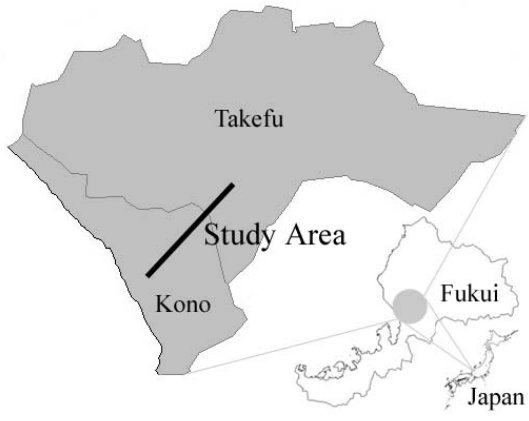

Fig. 1 Study Area

Table. 1 Specifications of TABI-320

Instrument Type	Pushbroom Thermal Imaging Microbolometer
Field of View (FOV)	48 deg across-track across 320 pixels; ~f/1
	0.25 deg along-track
Instantaneous Field of View	2.87 milliradians
Spectral Range	8 - 12 μm (800 - 1200 nm) : 1 band
Dynamic Range	4096 : 1 (12bits)
Temperature Range	-20 to 110 ℃ Nominal
NEΔt	0.1 K

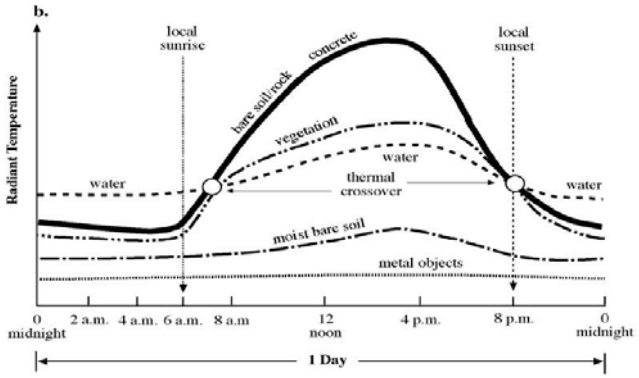

Fig. 3 Thermal Behavior of Materials in 1 Day
(From NASA's Website)

Table. 2 Flight Record of TABI

	GSD (m)	Altitude (ft)	Date	Course				Time (Local)	
				Start		End			
				Lat	Lon	Lat	Lon	Start	End
Early Afternoon (EA)	1.5	2425.0	2003/10/30	N 35°51'31.3"	E 136°08'13.7"	N 35°48'11.3"	E 136°05'23.6"	14:12:47	14:15:16
				N 35°51'34.0"	E 136°08'09.0"	N 35°48'14.0"	E 136°05'18.9"	14:24:59	14:27:28
Early in Morning (EM)			2003/10/31	N 35°48'11.3"	E 136°05'23.6"	N 35°51'31.3"	E 136°08'13.7"	8:33:53	8:36:23
				N 35°48'14.0"	E 136°05'18.9"	N 35°51'34.0"	E 136°08'09.0"	8:45:57	8:48:26

(a) Early Afternoon (EA) (b) Early Morning (EM)

Fig. 2 TABI Images with 1.5 m resolution on October 30-31, 2003

type. Thermal image has a great possibility for concrete monitoring because the deviation of concrete surface temperature in one day is large. We assume that the irregular distribution of temperature occurs at the concrete anomaly points.

4. DEFINITION OF CONCRETE ANOMALY

A report on the inspection activity of the concrete erosion structures in the study area by the Ministry of Construction, Japan in 1997 was utilized as a reference. The types of concrete structure problems in the report are listed below.

(1) Crack of Sprayed Mortar
(2) Peeling of Sprayed Mortar
(3) Swell of Sprayed Mortar
(4) Crack of Retaining Wall (Concrete Block)
(5) Swell of Retaining Wall (Concrete Block)

(6) Slight Shift of Retaining Wall (Concrete Block)
(7) Crack of Retaining Wall (Masonry)
(8) Swell of Retaining Wall (Masonry)
(9) Slight Shift of Retaining Wall (Masonry)

We defined the 9 types of concrete structure problems above as "concrete anomaly" in this study.

5. TEMPERATURE PATTERN OF NORMAL MATERIALS AND THE EFFECT BY SHADOW

In general, the radiant temperature observed by the spaceborne / airborne thermal sensors is easily affected by shadow, especially on the high resolution images. Therefore, a shadow simulation with DEM could be useful to estimate and remove its effect. However, the 50 m resolution DEM available in this study is insufficient to simulate the shadow area of the 1.5m GSD thermal images. Instead of DEM, 2 TABI images in early afternoon and in early morning were used to estimate the shadow effect.

The difference of the radiant temperature (ΔT) was defined as below.

$$\Delta T = T_{EA} - T_{EM} \quad (1)$$

Where T_{EA} is radiant temperature from the early afternoon (EA) image, T_{EM} is radiant temperature from the early morning (EM) image.

The average ΔT profile of four pure land cover types (Road, Vegetation, Concrete, Soil) are shown in Fig.4. Four shadow conditions shown in Table. 3 were sampled for each land cover type from the images. Each profile was taken from the averages of three lines of five pixels long (-2, 2).
For road, vegetation, and concrete, the ΔT pattern decreases from SM, NS, SB to SA. However, for soil, ΔT under NS is greater than that under SM. That is because the soil in shadow was still getting cooler at the data acquisition time for the EM image.

From Fig. 4, it can be seen that the trend of ΔT for road is similar to that for the concrete under all shadow conditions except for under NS as same as shown in Fig. 3. The difference in ΔT patterns between road and concrete under NS suggests a possibility for the discrimination of the two. ΔT for soil under NS is smaller than the value estimated from Fig. 3. This is reasonable as soil retains a certain amount of moisture.

The descending orders of ΔT by various conditions are Concrete, Road, Soil and Vegetation for NS; Road, Concrete, Vegetation and Soil for SM and SB; and Soil, Road, Concrete and Vegetation for SA. These orders could be a special characteristic of thermal behavior of materials, but the soil causes complication and will not be examined in detail here.

Fig. 5 shows the distribution of the radiant temperature in the

Table. 3 Shadow Conditions

Code	Shadow		Note
	EA	EM	
NS	N	N	No shadow in both observation time
SM	N	Y	Covered with shadow only in EM
SA	Y	N	Covered with shadow only in EA
SB	Y	Y	Covered with shadow in both observation time

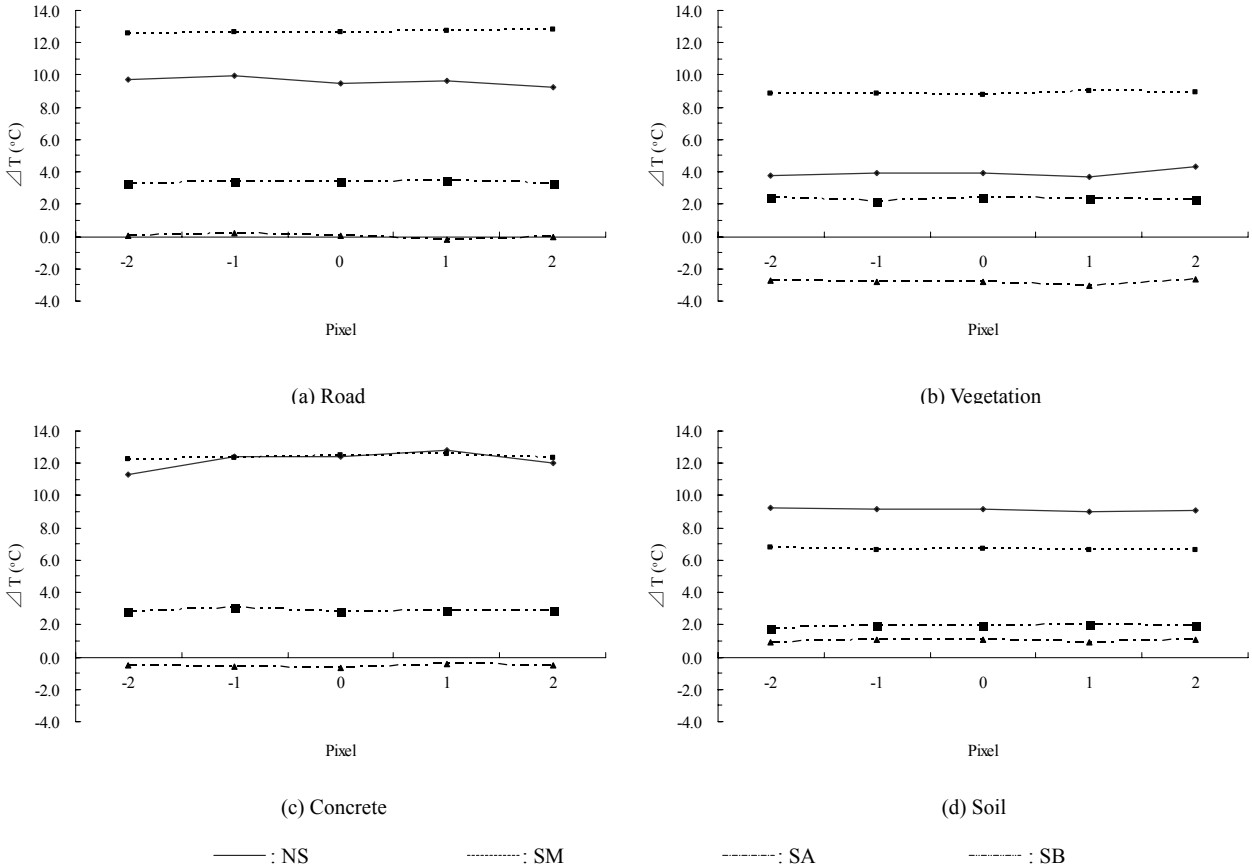

Fig. 4 Distribution of ΔT for Four Land Cover Types with Normal Condition

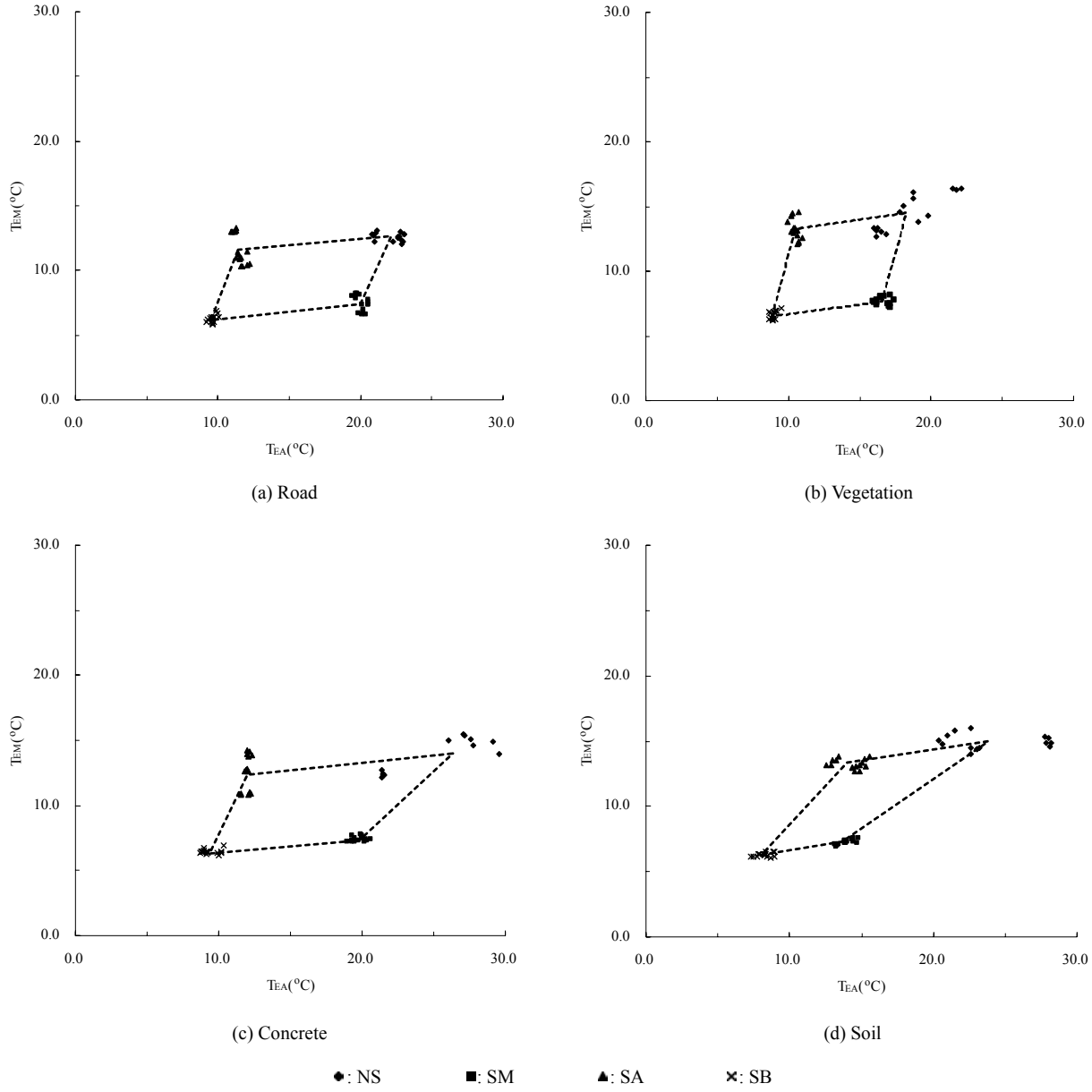

Fig. 5 Radiant Temperature Distribution of the Normal Land Cover Types under Four Shadow Conditions

Table. 4 Mean and Standard Deviation of the Radiant Temperature in Four Land Cover Types under Four Shadow Conditions

Land Cover Type	Radiant Temperature	NS		SM		SA		SB	
		MEAN	STD	MEAN	STD	MEAN	STD	MEAN	STD
Road	T_{EA}	22.20	0.88	20.10	0.35	11.52	0.37	9.63	0.22
	T_{EM}	12.59	0.31	7.43	0.58	11.57	1.11	6.26	0.27
	ΔT	9.61	1.01	12.68	0.80	0.02	1.46	3.36	0.24
Vegetation	T_{EA}	18.39	2.09	16.60	0.46	10.46	0.27	8.97	0.20
	T_{EM}	14.46	1.35	7.71	0.28	13.28	0.80	6.64	0.30
	ΔT	3.94	1.12	8.89	0.56	-2.81	0.98	2.31	0.28
Concrete	T_{EA}	26.35	3.80	19.79	0.45	11.99	0.20	9.36	0.56
	T_{EM}	14.05	1.21	7.42	0.19	12.53	1.28	6.45	0.17
	ΔT	12.19	2.82	12.39	0.52	-0.54	1.22	2.91	0.57
Soil	T_{EA}	24.03	2.92	13.91	0.53	14.24	0.94	8.24	0.48
	T_{EM}	14.91	0.54	7.24	0.19	13.24	0.37	6.29	0.16
	ΔT	9.13	2.99	6.66	0.39	1.00	1.06	1.94	0.44

four land cover types under the four shadow conditions. All points for calculation of the means shown in Fig. 4 are plotted in Fig. 5. The mean and standard deviation values of the radiant temperature of the four land cover types under various shadow conditions are shown in Table 4. T_{EA} under NS spreads more widely than those under other shadow conditions. T_{EM} under SA spreads more widely than those under other shadow conditions. The moisture on the ground seems to effect on the temperature distribution.

The dotted lines in Fig. 5 indicate the link of the mean radiant temperature under each shadow condition. The clusters of the four shadow conditions form a shape of a trapezoid. For road and vegetation, the shape is a parallelogram. There is a possibility for us to use the lengths of four sides and two diagonals of these trapezoids in pattern recognition. The result of further research will be reported elsewhere.

6. TEMPERATURE DISTRIBUTION OF CONCRETE ANOMALY AREA

As has been noted above, the shadow effect for the temperature distribution of materials under normal condition is quite complicated. Now we focus on the possibility of detecting the concrete anomaly. Although other techniques such as classification may be used, the irregular temperature pattern can

be found in the concrete anomalies.

Fig. 6 shows ΔT of the concrete including anomaly sites and the distribution of the concrete radiant temperature of these pixels is shown in Fig. 7. Four shadow conditions mentioned above were also sampled from the images. For each shadow condition, three lines of five pixel long were taken based on the inspection report in section 4. The five-pixel lines were sampled as follows: The points where the concrete structure problem were found in the check activities were sampled as the center pixel (pixel 0) and the four neighboring pixels (-2, -1, 1, 2) were sampled along the road direction (not along the slope aspect, for some pixels can be covered with vegetations). Each profile in Fig. 6 was taken from the averages of three lines.

ΔT under SM and that under SB are almost the same as those of normal concrete. On the other hand, ΔT under SA is larger and that under SN is smaller than those of normal concrete. These increase and decrease can be considered due to anomalies. It is likely that the concrete with anomalies keeps its temperature stable once it reaches a certain degree. Judging from the wide distribution of T_{EA}, the sampled pixels under no shadow may partly contain vegetation or other land cover types.

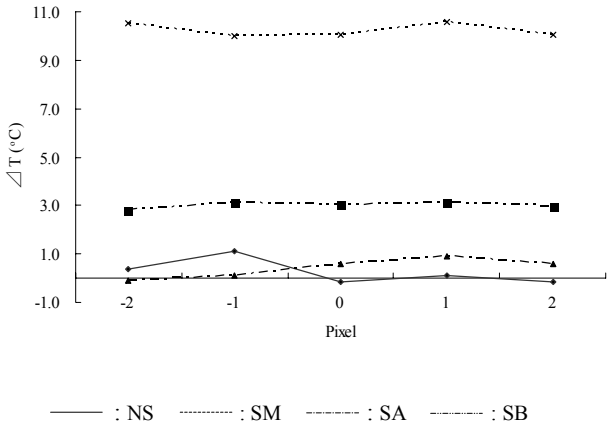

Fig. 6 Distribution of ΔT for Concrete Including Anomalies

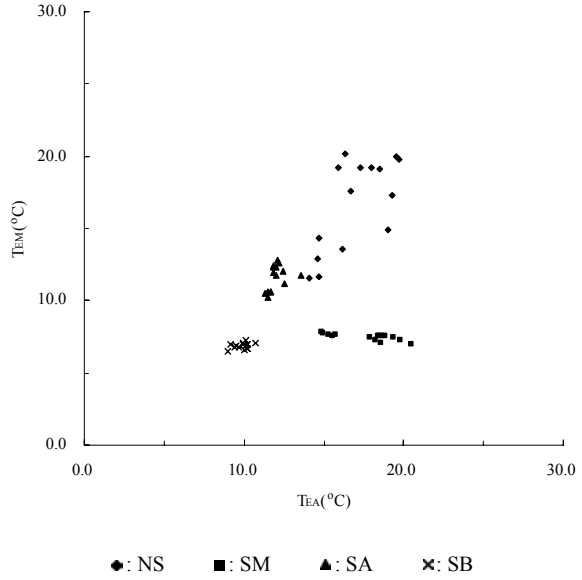

Fig. 7 Radiant Temperature Distribution of the Concrete Including Anomalies

The temperature distribution under SA and that under SB are also similar to those of normal concrete. It seems hard to detect the concrete anomaly under those shadow conditions from the temperature distribution. The temperature distribution range of the concrete with anomaly under NS is wider than that of normal concrete. It might be inferred from this distribution range that there are several types of concrete anomaly which can be detected by the thermal data. The distribution range of T_{EA} under SM is wider than that of normal concrete. It is not hard to imagine that the heat capacity of the concrete with anomaly is different from that of the normal one.

For a statistical interpretation of concrete anomaly, the T-test is proposed to detect the temperature anomaly at each pixel.

$$Z_{stnp} = X_{stnp} - M_{st} / \sigma_{st} \quad (2)$$

where Z : Statistical score
X : Radiant temperature of the pixel
M : Mean value of the radiant temperature of normal concrete (Shown in Tab.3)
σ : Standard deviation (STD) of the radiant temperature of normal concrete (Shown in Tab.3)
s : Shadow condition (N : NS, M : SM, A : SA, B : SB)
t : Observation time (A : EA, M : EM)
n : Number of line (1, 2, 3)
p : Pixel position (-2, -1, 0, 1, 2)

If $|Z_{sAnp}|$ or $|Z_{sMnp}|$ is greater than 1.96 (95% confidence interval), the pixel will be discriminated as a concrete anomaly point.

Table. 5 shows the results of T-test for the concrete anomaly points and the neighbor pixels. It can be seen that the irregular temperature is found not only at the pixel locations sampled as concrete anomaly pixel based on the report but also its neighbor pixels. 11 of 12 center pixels (Pixel 0) in the sampled lines were discriminated as concrete anomaly points. This accuracy presents that T-test is very appropriate for detecting the concrete anomaly. However, the results of the discrimination with (2)

Table. 5 Result of T-test for the Concrete Anomaly Points and the Neighbor Pixels

Shadow Condition	Line #	Time	Pixel				
			-2	-1	0	1	2
NS	1	EA	-1.87	-1.92	-2.54	-2.38	-2.08
		EM	2.64	0.72	2.95	4.26	4.21
	2	EA	-2.75	-2.63	-2.21	-1.80	-1.74
		EM	4.27	5.05	4.23	4.88	4.75
	3	EA	-3.23	-3.06	-3.09	-2.67	-3.07
		EM	-2.03	-1.94	-0.92	-0.41	0.23
SM	1	EA	-1.02	-3.09	-2.40	-2.87	-4.16
		EM	0.00	0.63	0.63	0.74	0.32
	2	EA	-2.60	-3.42	-2.02	1.51	0.09
		EM	-1.68	-0.79	0.47	-2.21	-0.95
	3	EA	-9.31	-8.96	-9.98	-10.71	-10.89
		EM	0.47	1.26	1.26	1.58	1.95
SA	1	EA	0.65	-0.55	2.55	8.10	2.35
		EM	0.24	-0.06	-1.02	-0.59	-0.41
	2	EA	-0.05	-0.60	1.10	-0.85	0.00
		EM	-0.13	-0.18	0.04	-0.45	-0.58
	3	EA	-3.25	-2.40	-2.65	-1.50	-1.40
		EM	-1.61	-1.82	-1.51	-1.51	-1.52
SB	1	EA	-0.39	0.21	0.52	0.11	-0.71
		EM	3.24	2.41	2.06	1.94	0.47
	2	EA	1.16	1.41	1.11	1.52	2.46
		EM	1.00	2.76	3.12	1.35	3.76
	3	EA	1.36	1.54	1.54	1.43	1.02
		EM	4.82	1.65	3.18	3.00	3.71

: Pattern.1 : $|Z_{sDnp}| >= 1.96$ and $|Z_{sMnp}| >= 1.96$
: Pattern.2 : $|Z_{sDnp}| >= 1.96$ and $|Z_{sMnp}| < 1.96$
: Pattern.3 : $|Z_{sDnp}| < 1.96$ and $|Z_{sMnp}| >= 1.96$

depend on M and σ because they are calculated from the pixels of the normal concrete.

The anomalies under NS are discriminated as pattern 1 or pattern 2 in table 5. On the other hand, those under SM and SA are discriminated as pattern 2 only and those under SB are mostly discriminated as pattern 3. These patterns don't directly imply any type of concrete anomalies, however, they can be a clue for further analysis of the relationship between concrete anomaly and its temperature distribution.

No pixel was discriminated as the concrete anomaly in line 2 under SA. The pixels like pixel -2 in line 1of NS, pixel 2 in line 2 of SB, and pixel -2 in line 3 of SM are judged as anomaly but are isolated. They might be mixels with vegetation or other land cover types.

Actually most of the pixels with concrete anomaly are mixels because the width of a crack or a peeling is within 3cm. The distribution trend of the temperature and the result of T-test suggest that airborne thermal remote sensing data is valid for detecting concrete anomaly.

7. CONCLUSIONS

In this paper, we examined the applicability of airborne thermal remote sensing data for concrete thermal mapping and anomaly detection. The shadow effect for the radiant temperature was measured. The distribution of 4 major land cover types without anomaly under several shadow conditions showed unique trends. Statistical T-test was proposed for the detection of concrete anomaly. The proposed method was capable. Airborne thermal remote sensing data with 1.5 m is insufficient for the detailed analysis of concrete anomalies, but the results indicate that there are great possibilities for detecting the anomaly position.

Future research directions include (1) shadow simulation with DTM of appropriate resolution to the image, (2) utilization of multitemporal and high resolution thermal images, (3) data fusion with optical remote sensing data and ancillary spatial information, and (4) development of algorithms for the detection of the concrete anomaly.

ACKNOWLEDGEMENTS

This paper is report 1 from a collaborative research plan between PASCO Corporation and the Center for the Assessment and Monitoring of Forest and Environmental Resources (CAMFER), University of California, Berkeley.

REFERENCES

Ben-Dor, E., Saaroni, H., 1997, Airborne video thermal radiometry as a tool for monitoring microscale structures of the urban heat island, International Journal of Remote Sensing, Vol.18, No.14, pp.3039-3053

Dare, P.M., et al., 2002, An operational application of automatic feature extraction: The measurement of cracks in concrete structures, Photogrammetric record, Vol.17, No.99, pp.453-464

Doihara, T., et al., 1998, Hierarchical image processing for crack measurement on concrete structures, Bulletin of Japan society of photogrammetry and remote sensing, Vol.37, No.3, pp.52-64 (In Japanese)

Gustavsson, T., 1999, Thermal mapping – a technique for road climatological studies, Meteorological Applications, Vol.6, pp.385-394

Nichol, J.E., 1996, High-resolution surface temperature patterns related to urban morphology in a tropical city: A satellite-based study, Journal of Applied Meteorology, Vol.35, No.1, pp.135-146

Qin, Z., Berliner, P., and Karnieli, A., 2001, A mono-window algorithm for retrieving land surface temperature from Landsat TM data and its application to Israel-Egypt border region, International Journal of Remote Sensing, Vol.22, No.18, pp.3719-3746

Quattrochi, D.A., Luvall, J.C., 1999, Thermal infrared remote sensing for analysis of landscape ecological processes: methods and applications, Landscape Ecology, Vol.14, No.6, pp. 577-598

Ramsey, M.S., Fink, J.H., 1999, Estimating silicic lava vesicularity with thermal remote sensing: a new technique for volcanic mapping and monitoring, Bulletin of Volcanology, Vol.61, No.1-2, pp.32-39